



# The H $\alpha$ Dots Survey. II. A Second List of Faint Emission-line Objects

John J. Salzer<sup>1</sup> , Jesse R. Feddersen<sup>1,2</sup> , Kathryn Derloshon<sup>1</sup>, Caryl Gronwall<sup>3,4</sup> , Angela Van Sistine<sup>1,5</sup>, Arthur Sugden<sup>1</sup>, Steven Janowiecki<sup>6</sup> , Alec S. Hirschauer<sup>7</sup> , and Jessica A. Kellar<sup>8</sup>

<sup>1</sup> Department of Astronomy, Indiana University, 727 East Third Street, Bloomington, IN 47405, USA; [josalzer@indiana.edu](mailto:josalzer@indiana.edu)

<sup>2</sup> Department of Astronomy, Yale University, P.O. Box 208101, New Haven, CT 06520, USA

<sup>3</sup> Department of Astronomy & Astrophysics, Pennsylvania State University, University Park, PA 16802, USA

<sup>4</sup> Institute for Gravitation & the Cosmos, Pennsylvania State University, University Park, PA 16802, USA

<sup>5</sup> Center for Gravitation, Cosmology, and Astrophysics, University of Wisconsin-Milwaukee, 3135 N Maryland Ave Milwaukee, Wisconsin 53211, USA

<sup>6</sup> University of Texas at Austin, McDonald Observatory, TX 79734, USA

<sup>7</sup> Space Telescope Science Institute, 3700 San Martin Dr., Baltimore, MD 21218, USA

<sup>8</sup> Department of Physics & Astronomy, Dartmouth College, Hanover, NH 03755, USA

Received 2020 August 18; revised 2020 September 14; accepted 2020 September 16; published 2020 November 3

## Abstract

We present the second catalog of serendipitously discovered compact extragalactic emission-line sources—H $\alpha$  Dots. These objects have been discovered in searches of moderately deep narrow-band images acquired for the ALFALFA H $\alpha$  project. In addition to cataloging 119 new H $\alpha$  Dots, we also present follow-up spectral data for the full sample. These spectra allow us to confirm the nature of these objects as true extragalactic emission-line objects, to classify them in terms of activity type (star-forming or AGN), and to identify the emission line via which they were discovered. We tabulate photometric and spectroscopic data for the all objects, and we present an overview of the properties of the full H $\alpha$  Dot sample. The H $\alpha$  Dots represent a broad range of star-forming and active galaxies detected via several different emission lines over a wide range of redshifts. The sample includes H $\alpha$ -detected blue compact dwarf galaxies at low redshift, [O III]-detected Seyfert 2 and Green Pea-like galaxies at intermediate redshifts, and QSOs detected via one of several UV emission lines, including Ly $\alpha$ . Despite the heterogeneous appearance of the resulting catalog of objects, we show that our selection method leads to well-defined samples of specific classes of emission-line objects with properties that allow for statistical studies of each class.

*Unified Astronomy Thesaurus concepts:* Galaxy abundances (574); Dwarf galaxies (416); Blue compact dwarf galaxies (165); Seyfert galaxies (1447); Quasars (1319); Starburst galaxies (1570); Star formation (1569); Emission line galaxies (459)

*Supporting material:* machine-readable tables

## 1. Introduction

Much of what we currently know about activity in galaxies—either extreme star formation events or nonstellar emission from Active Galactic Nuclei (AGN)—has been learned by studying systems that were originally recognized in focused surveys for such activity. These surveys have taken place at essentially all wavelengths, from the radio to X-rays. Ground-breaking surveys include the early 3C radio continuum surveys (Edge et al. 1959; Bennett 1962; Laing et al. 1983) and the Markarian objective-prism searches for UV-excess galaxies (e.g., Markarian 1967; Markarian et al. 1981).

Of particular relevance to the current study are the many surveys that have cataloged galaxies with strong optical emission lines, the so-called emission-line galaxies (ELGs). ELG surveys have tended to use one of two selection methods, although there are many variations on these two primary themes. The first utilizes objective-prism searches using wide-field Schmidt telescopes (e.g., MacAlpine et al. 1977; MacAlpine & Williams 1981; Sanduleak & Pesch 1982; Markarian et al. 1983; Pesch & Sanduleak 1983; Wasilewski 1983; Zamorano et al. 1994, 1996; Ugryumov et al. 1999; Hopp et al. 2000; Salzer et al. 2000, 2001, 2002). A key advantage of the objective-prism method is that it yields wide-field data, covering a substantial area in reasonable amounts of time. In addition, the spectral coverage of the prism typically allows for the detection of ELGs over a wide redshift range in a single exposure.

The second method involves the use of narrow-band filters to isolate the strong line emission in ELGs. Examples of surveys that utilize this latter method include Boroson et al. (1983), Kakazu et al. (2007), Cook et al. (2019). Narrow-band surveys typically employ smaller fields-of-view than objective-prism surveys, and are limited in their spectral range to the bandwidth of the filter or filters employed. They do, however, often result in deeper, more sensitive searches for ELGs.

The ELG survey presented in this study is of the latter type: narrow-band detection. We refer to our program as the H $\alpha$  Dots survey (Kellar et al. 2012) because we are searching for compact/unresolved sources of emission in images taken through narrow-band H $\alpha$  filters. The H $\alpha$  Dots survey is carried out utilizing a large set of narrow-band data obtained as part of a completely different program: the ALFALFA H $\alpha$  project (e.g., Van Sistine et al. 2016, hereafter *AHA*). The H $\alpha$  Dots program originated with the serendipitous discovery of unresolved emission-line sources in the *AHA* data. This initial effort resulted in our first survey list of 61 compact emission-line sources (Kellar et al. 2012).

The current paper presents the second list of H $\alpha$  Dots, which were discovered by searching narrow-band images from several additional *AHA* observing runs. As with the first H $\alpha$  Dots catalog, most of the work to analyze and select the faint emission-line sources was carried out by undergraduate students working with the senior author. Our paper is organized as follows: Section 2 describes the data used for the searches as well as our search methodology. Section 3 presents our new list

of objects, while Section 4 details our spectroscopic follow-up of the newly discovered ELGs. Section 5 presents key properties of the H $\alpha$  Dots, including their redshift distribution, spectroscopic properties, object classifications, luminosity and star formation rate (SFR) distributions, and metal abundances. Section 6 summarizes our main results. A standard  $\Lambda$ CDM cosmology with  $\Omega_m = 0.27$ ,  $\Omega_\Lambda = 0.73$ , and  $H_0 = 70 \text{ km s}^{-1} \text{ Mpc}^{-1}$  is assumed in this paper.

## 2. Observational Data and Search Technique

As mentioned earlier, the H $\alpha$  Dots survey is carried out using narrow-band images obtained for the AHA project (Van Sistine et al. 2016). The AHA project was a narrow-band imaging survey that observed a volume-limited sample of HI-detected galaxies cataloged in the ALFALFA survey (Giovanelli et al. 2005; Haynes et al. 2011, 2018). The primary goal of the AHA project was to study the star formation properties of a comprehensive sample of galaxies in the local universe, using the deep ALFALFA survey catalog as a source list. A total of 1555 galaxies were observed.

The AHA data consist of images obtained through both a continuum *R*-band filter and one of a set of narrow-band ( $\sim 60$ – $70 \text{ \AA}$  wide) H $\alpha$  filters. Two different narrow-band filter sets were employed (see Van Sistine et al. 2016), appropriate for galaxies with velocities up to  $\sim 9200 \text{ km s}^{-1}$ . Since the ALFALFA targets all have accurate redshifts from the HI detections, the appropriate narrow-band filter to use for each object was always clear.

Two telescopes were used for the AHA observations: the WIYN 0.9 m<sup>9</sup> and KPNO 2.1 m telescopes.<sup>10</sup> The current paper deals exclusively with images obtained with the WIYN 0.9 m telescope. All of the images were acquired with the S2KB CCD detector. We only read out the central  $1536 \times 1536$  pixels, which yielded a field-of-view of  $\sim 15.2$  arcmin square. A pair of 1200 s exposures obtained through the appropriate narrow-band filter were sandwiched around a 240 s *R*-band image for each target galaxy. Standard image processing procedures were applied to the data, after which the three images for a given galaxy were run through a custom pipeline to assign a world coordinate system and to scale and subtract the continuum *R*-band image from the narrow-band images (see Van Sistine et al. 2016).

Accurate flux calibration was essential for the AHA project. Multiple observations of spectrophotometric standard stars were carried out on each night of the program. On nights when conditions were not strictly photometric, the fields that were observed were flagged and re-observed on a later night using short “post-calibration” observations. All of the narrow-band fluxes that are measured from AHA images have a zero-point of the flux scale that is measured to better than 2% accuracy (and usually  $\sim 1\%$ ). Full details are included in Van Sistine et al. (2016).

<sup>9</sup> The 0.9 m telescope is operated by WIYN Inc. on behalf of a consortium of nine partner universities and organizations (see [www.noao.edu/0.9m/partners](http://www.noao.edu/0.9m/partners)). WIYN is a joint partnership of the University of Wisconsin at Madison, Indiana University, and the National Optical Astronomical Observatory.

<sup>10</sup> The KPNO 2.1 m telescope was formerly operated by the National Optical Astronomy Observatory (NOAO), which consisted of KPNO near Tucson, Arizona, Cerro Tololo Inter-American Observatory near La Serena, Chile, and the NOAO Gemini Science Center. NOAO was operated by the Association of Universities for Research in Astronomy (AURA) under a cooperative agreement with the National Science Foundation.

The H $\alpha$  Dot survey uses the fully processed images from the AHA project to search for point-like objects with an excess of emission in the narrow-band filter images. The search process is fully automated, and is described in detail by Kellar et al. (2012). In brief, the images for each field are scanned to identify all of the objects present in the field, after which the fluxes for each source are measured through the same small aperture in both the *R*-band and narrow-band images. Once the candidate H $\alpha$  Dots have been identified by our software, each potential dot is examined critically in the imaging data to weed out false detections (e.g., image artifacts).

Three selection criteria are used to identify potential H $\alpha$  dots. First, the narrow-band image must show an excess of flux over that measured in the continuum (*R*-band) image such that

$$\Delta m = m_{\text{NB}} - m_R \leq -0.4. \quad (1)$$

Here  $m_{\text{NB}}$  is the instrumental magnitude measured in the narrow-band filter, which includes both the line and continuum emission. This value of  $\Delta m$  corresponds to  $f_{\text{H}\alpha}/f_{\text{cont}} \approx 0.45$ . Given that the typical narrow-band filter used for the AHA project has a FWHM of  $\sim 70 \text{ \AA}$ , this implies an emission-line equivalent-width limit for detection of  $\sim 30 \text{ \AA}$ . Second, the ratio of the narrow-band flux excess to the formal uncertainty in that excess (both measured in magnitudes) must be

$$\text{ratio} = \Delta m / \sigma_{\Delta m} \geq 4.5. \quad (2)$$

The ratio parameter acts to exclude noisy sources from our catalog of candidates, serving a role similar to a traditional signal-to-noise limit. Third, each source must be extremely compact—either unresolved or marginally resolved in our images—to be selected. This latter criterion is somewhat subjective, but is meant to exclude extended galaxies with emission from disk H II regions. This criterion also means that we do not ever select the AHA target galaxy located within each field as an H $\alpha$  Dot.

Our automated selection process also finds dozens of H II regions in spiral disks and extended irregular galaxies. In particular, the AHA target galaxy in each of our fields is often detected multiple times because of its disk H II regions. These H II regions are identified during the visual examination of the computer-selected candidates and are cataloged separately. In general, the distinction between the H II regions and *bona fide* H $\alpha$  Dots is clear because most disk H II regions are located in the higher surface brightness portion of the stellar disk of their host galaxy. In cases where there is substantial separation between the apparent outer edge of the disk and the line-emitting source, we include the object in the list of H $\alpha$  Dots. We do not employ a rigorous criterion to select between the two options (H II region versus H $\alpha$  Dot), but in most cases the object must be at least 0.5 to 1.0 apparent disk radii beyond the outer edge of the galaxy to be included as an H $\alpha$  Dot. As described later on, several of these objects located at large radii are found through subsequent spectroscopy to be outlying H II regions of the nearby galaxy.

## 3. Second List of H $\alpha$ Dot Candidates

The AHA data for seven observing runs carried out on the WIYN 0.9 m telescope were searched for H $\alpha$  Dots following the methods described earlier. This represents a total of 354 fields with a total sky coverage of  $22.72 \text{ deg}^2$ . As a result of these searches 119 H $\alpha$  Dots were detected. The resulting

**Table 1**  
Second List of H $\alpha$  Dots

H $\alpha$ Dot #	R.A. degrees	decl. degrees	$\Delta m$	Ratio	$m_R$	NB Line Flux $\times 10^{-14}$ erg s $^{-1}$ cm $^{-2}$	$M_R$	log( $L(\text{H}\alpha)$ ) erg s $^{-1}$	log(SFR) $M_\odot$ yr $^{-1}$
(1)	(2)	(3)	(4)	(5)	(6)	(7)	(8)	(9)	(10)
62	138.33285	12.53536	−0.83	22.07	17.74 $\pm$ 0.04	1.030 $\pm$ 0.054	−16.53	39.80	−1.30
63 <sup>a</sup>	138.80328	11.88416	−1.54	5.00	20.96 $\pm$ 0.27	0.279 $\pm$ 0.032	−13.36	39.27	−1.83
64	138.84261	11.83980	−0.34	6.37	19.36 $\pm$ 0.08	0.187 $\pm$ 0.024	...	...	...
65	139.62692	13.77032	−1.52	10.35	20.04 $\pm$ 0.17	0.325 $\pm$ 0.028	−21.20	42.14	1.04
66	147.92081	14.10914	−0.63	13.92	18.91 $\pm$ 0.08	0.336 $\pm$ 0.029	−14.21	38.76	−2.34
67	149.25146	15.55564	−0.56	111.30	15.41 $\pm$ 0.03	5.982 $\pm$ 0.060	−18.58	40.94	−0.17
68	149.65731	15.43306	−1.82	17.51	20.12 $\pm$ 0.19	0.419 $\pm$ 0.032	...	...	...
69	149.67200	15.40155	−0.71	13.30	18.15 $\pm$ 0.08	0.427 $\pm$ 0.027	−16.01	40.12	−0.98
70	159.09391	13.63132	−0.87	14.70	20.05 $\pm$ 0.05	0.191 $\pm$ 0.015	−21.19	42.52	...
71	171.07641	14.31403	−0.40	6.58	18.85 $\pm$ 0.09	0.168 $\pm$ 0.030	−22.44	40.83	...
72	174.32659	15.50637	−1.05	22.92	19.26 $\pm$ 0.05	0.518 $\pm$ 0.021	−22.05	42.86	1.75
73 <sup>a</sup>	175.48027	15.94398	−0.63	6.10	19.29 $\pm$ 0.10	0.196 $\pm$ 0.047	−21.89	42.20	1.10
74	177.07405	12.71669	−2.23	9.59	21.25 $\pm$ 0.25	0.371 $\pm$ 0.025	−12.48	39.60	−1.51
75	181.35257	15.41589	−0.82	6.11	20.64 $\pm$ 0.12	0.091 $\pm$ 0.019	−27.55	...	...
76	209.48133	14.43082	−1.46	21.46	20.75 $\pm$ 0.06	0.243 $\pm$ 0.013	−20.51	42.55	1.45
77	349.83866	26.13977	−0.96	79.89	16.93 $\pm$ 0.03	3.053 $\pm$ 0.061	−17.07	40.25	−0.85
78 <sup>a</sup>	10.15819	27.04192	−1.95	6.24	21.43 $\pm$ 0.32	0.263 $\pm$ 0.030	−13.12	39.33	−1.77
79	11.15322	26.92934	−1.35	51.10	18.43 $\pm$ 0.04	1.524 $\pm$ 0.042	−16.07	40.07	−1.03
80	1.63913	27.24681	−0.52	7.96	19.82 $\pm$ 0.05	0.153 $\pm$ 0.018	−28.49	...	...
81	2.03670	27.45397	−1.66	46.27	18.85 $\pm$ 0.04	1.653 $\pm$ 0.042	−15.50	40.12	−0.98

**Note.** Table 1 is published in its entirety in the machine-readable format. A portion is shown here for guidance regarding its form and content.

<sup>a</sup> Indicates duplicate detections: H $\alpha$  Dot 63 = H $\alpha$  Dot 108; H $\alpha$  Dot 73 = H $\alpha$  Dot 30; H $\alpha$  Dot 78 = H $\alpha$  Dot 47; H $\alpha$  Dot 86 = H $\alpha$  Dot 51; H $\alpha$  Dot 109 = H $\alpha$  Dot 148; H $\alpha$  Dot 129 = H $\alpha$  Dot 49; H $\alpha$  Dot 160 = H $\alpha$  Dot 43.

(This table is available in its entirety in machine-readable form.)

surface density of H $\alpha$  Dots is 5.24 deg $^{-2}$ , virtually identical to the density of Dots found in Kellar et al. (2012) of 5.22 deg $^{-2}$ .

Table 1 presents our second catalog of H $\alpha$  Dot candidates. The first column in the table is the H $\alpha$  Dot number. Following the convention established in Kellar et al. (2012), the H $\alpha$  Dot candidates are numbered sequentially in R.A. (RA) order for all objects found from the search of the fields from a given AHA observing run. For example, the search of the data obtained in March 2008, the first of the AHA observing runs considered in the current catalog, yielded 15 dot candidates. These were ordered by RA and numbered 62–76 because the previous list ended with H $\alpha$  Dot 61. Following the dot number, RA and Dec (J2000) are given in columns 2 and 3. The coordinates listed are typically those measured by the Sloan Digital Sky Survey (York et al. 2000; Abolfathi et al. 2018), as we found that the SDSS astrometry was typically more reliable than our own.

The selection parameters  $\Delta m$  and ratio are listed in columns 4 and 5, and were defined in the previous section. Column 6 lists the measured  $R$ -band magnitude of each source as obtained from our continuum images. Comparison between our photometry and the  $r$ -band magnitudes from SDSS generally show good agreement. Column 7 presents the emission-line flux measured from the continuum-subtracted narrow-band images. The narrow-band fluxes are calibrated using spectrophotometric standard stars obtained nightly as part of the AHA survey. We note that these emission-line fluxes are *not* H $\alpha$  fluxes in all cases. As discussed in Section 4 and Section 5, for many of the objects in our survey, the emission line detected is a line other than H $\alpha$ .

The final three columns in Table 1 are derived properties of the H $\alpha$  Dots. We present the  $R$ -band absolute magnitude in column 8, the H $\alpha$  luminosity in column 9, and the H $\alpha$ -based SFR in column 10. All three quantities make use of the

spectroscopic redshifts presented in Section 4. We discuss these derived properties in detail in Section 5.4.

Images of three example H $\alpha$  Dots are shown in Figure 1. In each example, the left-hand image is a cut-out of our  $R$ -band continuum image, the middle image is the same field imaged with the relevant narrow-band filter, and the right-hand image shows the continuum-subtracted image. All image sections are  $2.0 \times 2.0$  arcminutes square. These three objects were selected because they illustrate the three principal line-selection groups discussed in Section 4. The top row shows the H $\alpha$ -detected star-forming galaxy H $\alpha$  Dot 81, the middle row displays the [O III]-detected galaxy H $\alpha$  Dot 135, while the bottom row presents the Ly $\alpha$ -detected QSO H $\alpha$  Dot 80. All three of these objects also have spectra that are shown in Figures 3–5. While all three objects clearly show excess emission in the continuum-subtracted images (right-hand column), it is not possible to ascertain the galaxy activity type or which emission line was present in the survey narrow-band filter by examination of the images alone.

Figure 2 presents histograms of the two principal observables from the imaging survey data: emission-line flux and  $R$ -band apparent magnitude. In both plots, we show the cumulative distributions from both of the survey lists. The red-lined histogram shows the measured values for all 180 H $\alpha$  Dots, while the blue cross-hatched histograms show the same parameters for the 18 false detections. The latter were identified after completion of the follow-up spectroscopy described in Section 4.

The distribution of emission-line flux is shown in the left-hand panel, and exhibits a median value of  $2.3 \times 10^{-15}$  erg s $^{-1}$  cm $^{-2}$ . The flux distribution rises until  $\sim 1.3 \times 10^{-15}$  erg s $^{-1}$  cm $^{-2}$ , beyond which it drops off precipitously. This flux level can be taken as an *approximate* line flux



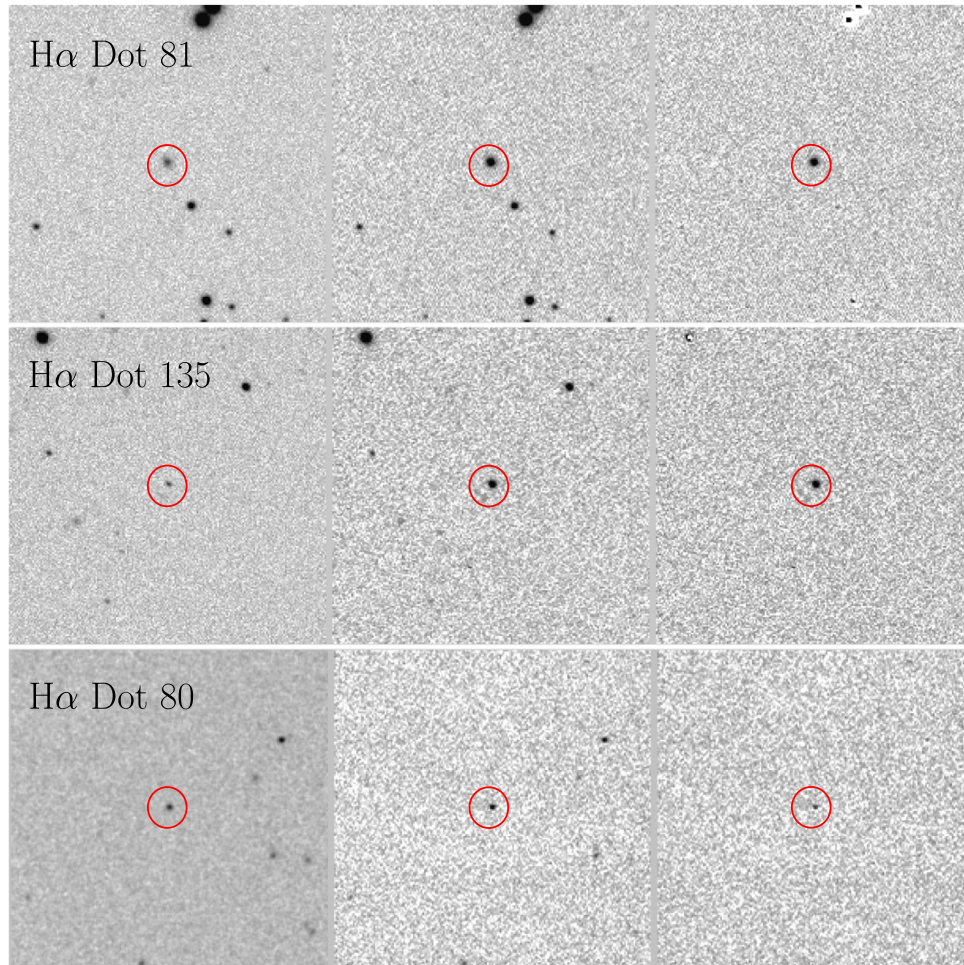


**Figure 1.** Example images of H $\alpha$  Dots cataloged in this study. In all three examples, the left-hand image is a cut-out of the  $R$ -band continuum image, the central image is taken through the relevant narrow-band filter, and the right-hand image is the continuum-subtracted image. Each image section shows a  $120 \times 120$  arcsec FOV. Top: H $\alpha$  Dot 81 is an H $\alpha$ -detected dwarf star-forming galaxy with  $R = 18.85$ ,  $M_R = -15.5$ , and  $z = 0.0153$ . Middle: H $\alpha$  Dot 135 is an [O III]-detected Green Pea (GP)-like galaxy with  $R = 20.17$ ,  $M_R = -21.3$ , and  $z = 0.3294$ . Bottom: H $\alpha$  Dot 80 is a QSO detected by its Ly $\alpha$  line. It has  $R = 19.82$ ,  $M_R = -28.5$ , and  $z = 4.4937$ . All three objects shown here have spectra displayed in Section 4.

completeness limit for the sample. It should be stressed that the detection of an emission-line source in a narrow-band survey such as this depends on a number of factors, including line flux, line equivalent width (e.g., the contrast between the line and the underlying stellar continuum), and redshift. Despite the complicated selection function, the flux value associated with the peak of the histogram can still serve as a first-pass estimate of the survey depth. The faintest “real” objects that have been detected have line fluxes of  $\sim 6 \times 10^{-16}$  erg s $^{-1}$  cm $^{-2}$ . Not surprisingly, the false detections are nearly all found among the lowest flux objects in the survey. Only one has a measured line flux within the brighter half of the sample.

The  $R$ -band apparent magnitude distribution is shown in the right-hand panel of Figure 2. The overall brightness range of the sample is quite large, extending from  $R = 15$  to  $R = 23$ , with a median value of  $R = 19.84$ . The false detections once again tend to be located among the fainter half of the overall distribution. However, this tendency is not nearly as strong as seen in the line flux plot, which is a clear indication that the sample is not a magnitude-limited one. Fully 23 out of the 26 objects with  $R > 21.0$  are *bona fide* emission-line objects, including all six with  $R > 22.0$ . We consider this to be an impressive result considering that the survey was carried out on a 0.9 m telescope.

Due to the overlap of some of the AHA survey fields, several H $\alpha$  Dots have been detected more than once with images taken on separate observing runs. This includes five objects in the current survey list that were previously cataloged in Kellar et al. (2012), plus two additional sources that were found in data obtained on different observing runs covered by the current searches. Since these duplicate detections represent discoveries made from independent data, we decided to retain them in our catalog for completeness. Hence, our current catalog includes only 112 unique H $\alpha$  Dots. All duplicate H $\alpha$  Dots are labeled as such in Table 1. In the subsequent discussions and figures, these duplicate sources will appear only once.

#### 4. Follow-up Spectroscopy of the New H $\alpha$ Dot Candidates

Once an H $\alpha$  Dot candidate is detected in the narrow-band images, it is placed into a queue for follow-up spectroscopy. Until a spectrum is obtained for an H $\alpha$  Dot candidate, it remains just that: a candidate. Furthermore, without a follow-up spectrum, we have no idea about which emission line was responsible for the detection, or what class of activity the H $\alpha$  Dot belongs to (e.g., star-forming or AGN). Hence, the

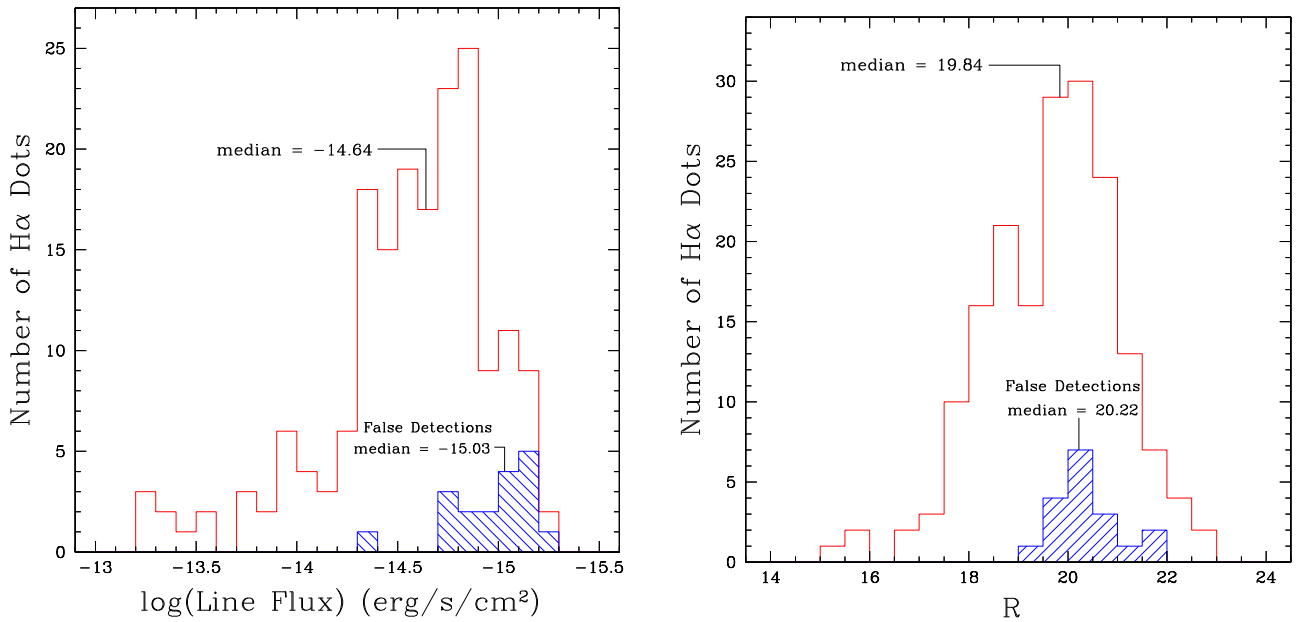


**Figure 2.** (Left-hand panel) Composite emission-line flux distribution for the first two lists of H $\alpha$  Dots ( $N = 180$ ). The line flux is measured directly from our narrow-band images. The specific emission line being measured is only revealed through spectroscopic follow-up. The blue cross-hatched histogram shows the line flux distribution of the 18 false detections. The latter distribution is heavily weighted toward the faintest fluxes detected by our survey. (Right-hand panel) Composite  $R$ -band magnitude distribution for the first two lists of H $\alpha$  Dots ( $N = 180$ ). The median apparent magnitude of  $R = 19.84$  is indicated. The blue cross-hatched histogram shows the magnitude distribution for the 18 false detections; the majority of these objects are included in the fainter half of the overall sample.

acquisition of a follow-up spectrum is essential to both verify and understand the nature of each candidate.

For all of the H $\alpha$  Dots in the current study, follow-up “first-look” spectra were obtained using the Hobby-Eberly 9.2 m telescope<sup>11</sup> (HET) that is located at the McDonald Observatory. All observations were carried out in queue mode by the resident HET observers. As H $\alpha$  Dots were cataloged they were forwarded to the HET queue to await observation, usually with a one year time lag. All of these “first-look” spectra were taken with short exposure times of 10 minutes each.

All spectral data were obtained with the Marcario low-resolution spectrograph (LRS; Hill et al. 1998). Initially, each candidate was observed in the wavelength region 4350–7250 Å using LRS grating G2. The G2 spectra have a reciprocal dispersion of 2.00 Å pixel<sup>-1</sup> and a pixel scale of 0.47 arcsec along the slit (for the default case of  $2 \times 2$  pixel binning). These data provided coverage of the spectral region containing the emission line detected in the narrow-band filter images and allowed for the determination of the redshift of each source. In the cases where the H $\alpha$  Dot was detected via the H $\alpha$  line, this was the only spectrum obtained. Galaxies detected by the [O III]  $\lambda$ 5007 line were left in the queue to be observed with the G3 grating. The purpose of the G3 spectra was to observe redshifted H $\alpha$  and the [N II]  $\lambda\lambda$  6383,6548 doublet. The G3 grating delivered spectra that covered the wavelength range 6300–9100 Å at 1.91 Å pixel<sup>-1</sup>. [O II]-detected galaxies were also observed with the G3 grating, giving us access to their [O III] and H $\beta$  lines. All spectra were obtained using a 2 arcsecond wide slit.

Data processing followed standard practice, and all data reduction was carried using IRAF. The spectral images had

their bias levels removed using overscan fitting, after which an averaged bias image was subtracted to remove any two-dimensional structure. Flat-field frames were combined into a single image, normalized, and then applied to the science images. Particle events on the detector were eliminated using LACOS\_SPEC (van Dokkum 2001). Next the spectra were extracted to a one-dimensional format and sky subtracted. Wavelength calibrations were provided using spectra of Ne and Cd lamps, and a single spectrophotometric standard star observed nightly was used to perform a relative flux calibration. The emission lines present in the fully reduced spectra were measured using the IRAF routine SPLAT.

All of the H $\alpha$  Dots listed in Table 1 have been observed spectroscopically. We tabulate relevant information derived from our spectra in Table 2. Column 1 lists the H $\alpha$  Dot number while column 2 specifies the activity type of each object: SFG = star-forming galaxy, H II = outlying/isolated H II region, Sy1 = Seyfert 1 galaxy, Sy2 = Seyfert 2 galaxy, QSO = quasi-stellar object, and NoELG = a false detection whose spectrum displays no emission lines. The criteria used to place each H $\alpha$  Dot into the appropriate activity class are discussed in Section 5.2 and Section 5.3. Column 3 gives the observed redshift  $z$ , and column 4 lists the decimal reddening coefficient  $c_{H\beta}$ , nearly always derived from the observed H $\alpha$ /H $\beta$  ratio. In a few cases of higher-redshift systems where H $\alpha$  is not observed, we use the H $\gamma$ /H $\beta$  ratio instead. Negative values of  $c_{H\beta}$  are treated as zero when correcting the emission-line ratios for reddening. Columns 6 and 7 give the measured equivalent widths of the H $\alpha$  and [O III]  $\lambda$ 5007 lines, respectively (in Å). The next four columns (7–10) list the logarithms of the specified ratios of emission-line fluxes. The line ratios have all been corrected for reddening using the value of  $c_{H\beta}$  given in column 4. Many of the line ratios that are indicated are unavailable for a given object because the wavelength coverage of our spectra is fixed but the redshifts of the objects vary over a huge range. Finally, column 11 lists the derived oxygen

<sup>11</sup> Based on observations obtained with the Hobby-Eberly Telescope, which is a joint project of the University of Texas at Austin, the Pennsylvania State University, Stanford University, Ludwig-Maximilians-Universität München, and Georg-August-Universität Göttingen.

**Table 2**  
H $\alpha$  Dots: Measured Spectral Properties

H $\alpha$ Dot # (1)	ELG Type (2)	$z$ (3)	$c_{H\beta}$ (4)	EW H $\alpha$ (5)	EW [O III] (6)	[N II]/H $\alpha$ (7)	[O III]/H $\beta$ (8)	[O II]/H $\beta$ (9)	[S II]/H $\alpha$ (10)	$\log(\text{O}/\text{H})+12$ (11)
62	SFG	0.0163	-0.02	64.4	64.2	-1.51	0.57	...	-0.86	8.03
63	H II	0.0169	0.40	85.9	48.4	-0.71	0.45	...	-0.55	8.55
64	NotELG	...	...	...	...	...	...	...	...	...
65	SFG	0.3243	0.24	369.2	360.7	-1.26	0.64	0.37	-0.72	8.15
66	SFG	0.0098	-0.17	40.8	23.0	-1.05	0.32	...	...	8.44
67	SFG	0.0145	0.74	37.4	3.9	-0.47	-0.40	...	-0.50	8.97
68	NotELG	...	...	...	...	...	...	...	...	...
69	SFG	0.0157	0.54	22.1	5.9	-1.22	0.20	...	-0.53	...
70	Sy2	0.3239	0.69	63.5	126.8	-0.19	0.92	0.57	...	...
71	Sy2	0.3313	...	13.8	19.1	-0.46	1.41	1.12	...	...
72	SFG	0.3325	0.47	...	125.8	...	0.38	0.57	...	...
73	SFG	0.3173	0.31	123.2	69.3	-1.25	0.45	0.46	-0.48	8.27
74	H II	0.0128	0.73	1319.0	603.1	-0.96	0.43	...	-0.81	8.44
75	QSO	4.4637	...	...	...	...	...	...	...	...
76	SFG	0.3299	0.53	224.0	220.4	-1.26	0.54	0.55	...	8.21
77	SFG	0.0125	0.20	46.8	21.9	-0.82	0.25	...	-0.49	8.59
78	SFG	0.0170	0.09	1706.0	646.6	-1.67	0.55	...	-1.21	7.94
79	SFG	0.0168	0.05	177.4	131.9	-1.44	0.51	...	-0.77	8.12
80	QSO	4.4937	...	...	...	...	...	...	...	...
81	SFG	0.0153	0.18	364.8	562.7	-1.64	0.77	...	-1.15	7.80

**Note.** Table 2 is published in its entirety in the machine-readable format. A portion is shown here for guidance regarding its form and content.

(This table is available in its entirety in machine-readable form.)

abundance, given in the standard nebular scale of  $\log(\text{O}/\text{H}) + 12$ . A description of how the abundances are derived is given in Section 5.

Plots displaying example spectra are shown in Figure 3–5. We separate the spectra into the three principal line-selection categories present in the survey: H $\alpha$  detection, [O III] detection, and detection via a UV emission line. The spectral coverage of the narrow-band filters used for the survey was between 6595 and 6734 Å, so the specific emission line responsible for the detection of each H $\alpha$  Dot is usually immediately apparent from its spectrum.

Figure 3 illustrates three H $\alpha$ -detected sources. Objects detected via the H $\alpha$  line are the most common type of H $\alpha$  Dot. In all three cases, the spectra show strong [O III] $\lambda\lambda$  4959,5007 lines and weak [N II] $\lambda\lambda$  6548,6583 lines, which is indicative of metal-poor galaxies. Unfortunately, the spectral range provided by the HET LRS set-up used does not cover the important [O II] $\lambda\lambda$  3726,3729 doublet for the low redshifts of the H $\alpha$ -detected H $\alpha$  Dots. Two of the galaxies illustrated—H $\alpha$  Dot 81 and 174—are blue compact dwarfs (BCDs), with  $R$ -band absolute magnitudes of  $-15.5$  and  $-15.2$ , respectively. Both exhibit the very compact morphology characteristic of BCDs. The third, H $\alpha$  Dot 127, represents a luminous H II region located on the edge of a very low surface brightness disk. The disk was not detected in our short  $R$ -band survey images, which is why it was classified as an H $\alpha$  Dot. H $\alpha$  Dot 127 is still a very dwarf system ( $M_R = -16.0$ ). A more complete evaluation of the properties of the H $\alpha$ -detected objects is presented in the following section.

Detections via the [O III] $\lambda$ 5007 line account for the second largest subsample of objects cataloged in the H $\alpha$  Dot survey. Figure 4 shows the spectra of three [O III]-detected objects. The top spectrum is of H $\alpha$  Dot 76, which is a star-forming galaxy with  $M_R = -20.5$  that appears to be part of a merger system. The spectrum of H $\alpha$  Dot 135 (middle) exhibits the

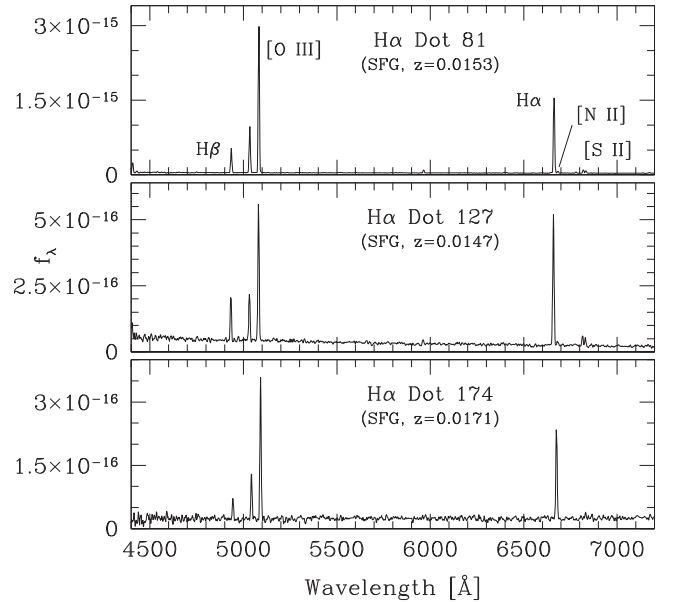


**Figure 3.** Example spectra of H $\alpha$  Dot galaxies. The three spectra included in this figure are all low redshift H $\alpha$ -detected star-forming systems. They are all dwarf galaxies and have low metallicities.

characteristics of the GP galaxies (e.g., Cardamone et al. 2009; Brunker et al. 2020), and in fact looks like a GP in the SDSS color images. With an [O III] $\lambda$ 5007 equivalent width of  $\sim 1000$  Å and a very compact appearance (unresolved in our images) it certainly appears to be a true GP. Finally, the lower spectrum in Figure 4 is that of the Seyfert 2 galaxy H $\alpha$  Dot 159. The similarities between this spectrum and the one directly above it in Figure 4 illustrate the importance of having the G3 spectra that cover the H $\alpha$  plus [N II] $\lambda\lambda$  6548,6583 lines. It is the H $\alpha$ /[N II] ratio that clearly delineates this galaxy as a Seyfert 2 (see Sections 5.2 and 5.3 for details of our



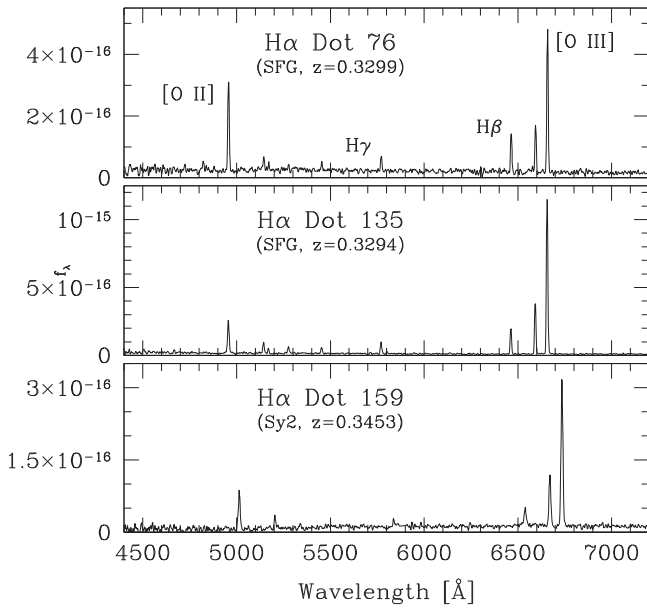


**Figure 4.** Example spectra of three [O III]-detected H $\alpha$  Dots. In all three cases, we possess additional spectra that reach further to the red and include the H $\alpha$  and [N II] lines. This allows us to unambiguously classify the galaxies as either star-forming or AGN. The upper two spectra illustrate SFGs, with H $\alpha$  Dot 135 exhibiting properties similar to the GP galaxies, while the bottom spectrum is that of a Seyfert 2 galaxy.

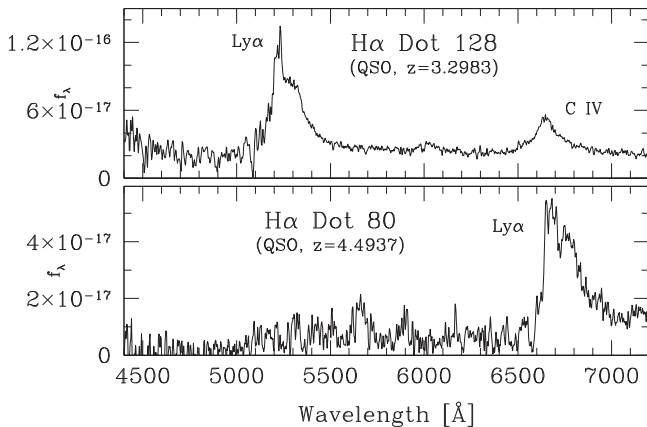


**Figure 5.** Spectra of two QSOs detected in the H $\alpha$  Dot survey. The upper spectrum represents a  $z = 3.2983$  QSO that was detected via its strong C IV  $\lambda 1549$  line; Ly $\alpha$  is also present. The lower spectrum illustrates a Ly $\alpha$ -detected QSO with  $z = 4.4937$ .

classification criteria). H $\alpha$  Dot 159 has an  $R$ -band absolute magnitude of  $-21.1$ .

Figure 5 shows two spectra of higher-redshift H $\alpha$  Dots that were detected by one of the strong UV lines typically seen in the spectra of QSOs. The top spectrum is that of H $\alpha$  Dot 128, a QSO detected via its C IV  $\lambda 1549$  line at  $z = 3.30$ , while the lower spectrum is that of the Ly $\alpha$ -detected QSO H $\alpha$  Dot 80 ( $z = 4.49$ ). Even though the UV-line-detected component of the survey is small ( $\sim 7\%$ ), we consider it to be an impressive accomplishment of the narrow-band selection technique that we are sensitive to  $z = 4$  QSOs using a 0.9 m telescope.

Nine of the objects in our second catalog of H $\alpha$  Dots did not exhibit any emission lines in their follow-up spectra, and are labeled as false detections in Table 2. This represents a false positive rate of 7.6%, which is roughly half of the value from the first survey list. We used the results from the first survey to

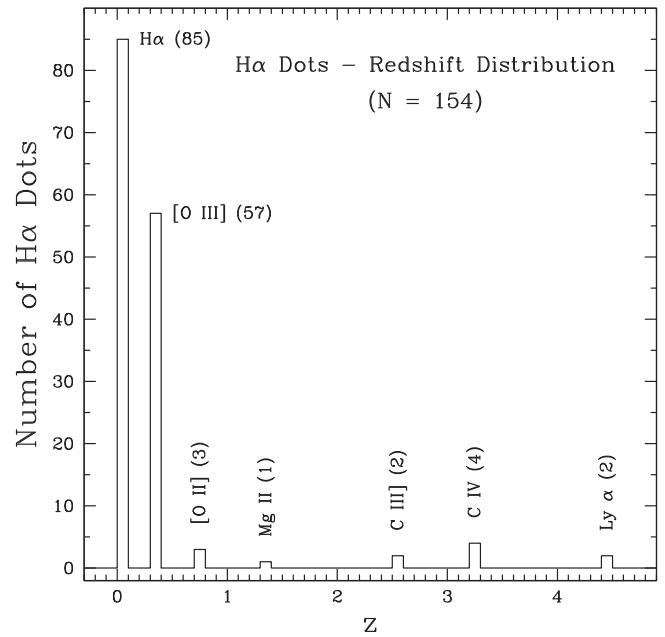


**Figure 6.** Redshift distribution of the H $\alpha$  Dots from the first two survey lists ( $N = 154$  unique objects). Each peak in the plot represents a specific emission line that has shifted into the bandpass of the filters used from the ALFALFA H $\alpha$  survey.

improve upon our selection method, resulting in this dramatic drop in false positives. In most cases, the false detections are objects with line fluxes close to our sensitivity limit (Figure 2), although in a few instances they were caused by image artifacts that escaped attention during our visual checks of the candidates. Of the nine false detections in the current catalog, four are galactic stars and five are galaxies.

## 5. Discussion

### 5.1. Redshifts

The narrow-band selection technique employed in the H $\alpha$  Dots survey naturally leads to the detection of discrete classes of emission-line objects in well-defined redshift ranges. In this subsection, we examine the redshift distribution of the H $\alpha$  Dots, while in the following subsection we utilize the spectroscopic data to classify each object into one of a handful of specific groups. Throughout the remainder of this paper, we combine the H $\alpha$  Dots cataloged in both the first survey list (Kellar et al. 2012) and those discovered in the current work to take advantage of the larger sample of objects. Our evaluation suggests that there are no fundamental differences between the properties of the objects from the two catalogs.

Figure 6 displays the observed redshift distribution for the H $\alpha$  Dots from both survey lists. There are 154 unique objects included rather than 180. The difference is accounted for by the 18 false detections in the first two lists and the eight duplicate objects found in the analysis of independent survey images. The redshift distribution is displayed with a very coarse sampling on purpose, so that the height of each bin represents the number of objects detected via a specific emission line.

By far the most common lines used in the discovery of the H $\alpha$  Dots are H $\alpha$  and [O III]  $\lambda 5007$ . The H $\alpha$  line accounts for 85 out of the 154 unique ELGs cataloged in the first two lists (55%). The H $\alpha$ -detected sources fall within the redshift range 0.0056–0.0243 (velocity range 1690–7430 km s $^{-1}$ ). As

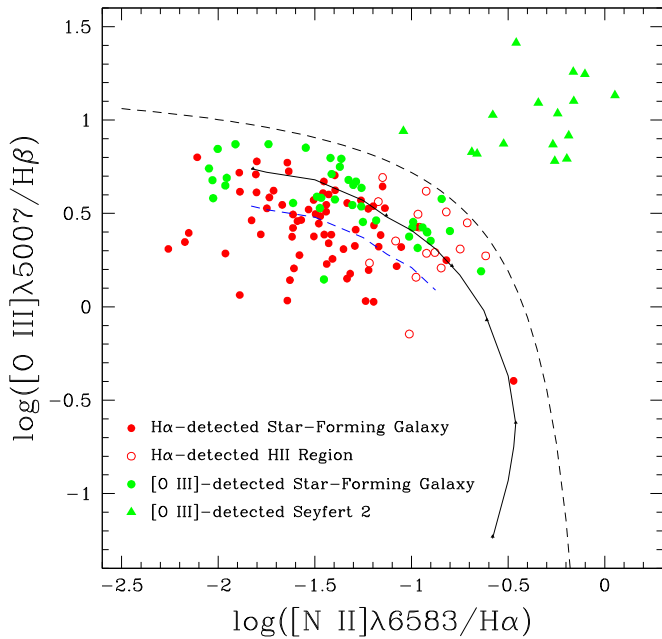


**Figure 7.** Emission-line diagnostic diagram for the full sample of  $H\alpha$  Dots. This figure includes 138 out of the 154 unique, *bona fide* Dots, excluding the broad-lined AGN (QSOs and Seyfert 1s), as well as four galaxies that lack detection of both line ratios plotted. The solid line shows a locus of theoretical model points taken from Dopita & Evans (1986), where the assumed metallicity of the gas decreases along the model curve from the lower right ( $2\times$  solar abundance) to the upper left ( $0.25\times$  solar abundance). The black-dashed line shows the empirical boundary between stellar and nonstellar photoionized objects (Kauffmann et al. 2003). The meaning of the blue-dashed line is discussed in Section 5.4. The significance of the locations of each of the four classes of objects displayed are discussed in the text.

discussed later on, they are predominantly low-luminosity systems. The  $[O III]\lambda 5007$ -detected  $H\alpha$  Dots represent an additional 57 sources (37% of the sample). To be detected via the  $[O III]\lambda 5007$  line using our survey filters, objects need to be in the redshift range 0.316–0.349 (distances of 1660–1875 Mpc). This in turn requires them to be fairly luminous systems to be detected.

The remaining 12  $H\alpha$  Dots are higher-redshift systems that were detected via one of several UV emission lines. Three sources were detected by the  $[O II]\lambda 3727$  doublet, and have redshifts between 0.78 and 0.80. Based on our G3 spectra of these galaxies, we classify two as AGN and one as star-forming (see Sections 5.2 and 5.3 for classification details). The remaining nine high-redshift  $H\alpha$  Dots are all broad-lined QSOs. These include one object detected via its  $Mg II (\lambda 2798)$  doublet ( $z = 1.35$ ), two found by the semi-forbidden  $C III] \lambda 1909$  line ( $z = 2.49$ – $2.55$ ), four detected from strong  $C IV (\lambda 1549)$  at  $z$  between 3.28 and 3.30, and two via  $Ly\alpha$  emission ( $\lambda 1215$ ) with redshifts of 4.46 and 4.49 (see Figure 5). While the higher-redshift sources make up only 8% of the overall sample, they represent interesting sources and emphasize the power of the narrow-band detection method for detecting faint, high-redshift objects.

### 5.2. Spectroscopic Diagnostics

We can learn much about the nature of our Dots by considering the information presented in their emission-line spectra. In particular, we can utilize an emission-line ratio diagnostic diagram (e.g., Baldwin et al. 1981; Veilleux & Osterbrock 1987, hereafter BPT diagram) using the measured strengths of key emission lines to help distinguish between

different types of objects. Figure 7 displays such a BPT diagram for the  $H\alpha$  Dots, plotting the logarithm of the  $[O III]\lambda 5007/H\beta$  ratio against the logarithm of the  $[N II]\lambda 6583/H\alpha$  ratio.

We display the objects detected with the  $H\alpha$  line in red and objects detected via  $[O III]\lambda 5007$  in green in Figure 7. We further subdivide both groups. For the  $H\alpha$  sources, we distinguish between objects that are distinct star-forming galaxies (solid red dots) and those that are outlying H II regions near large disk galaxies (red circles). The latter are usually located well outside the apparent optical disk of the host galaxy (see below). The outlying H II regions as a class tend to be located among the more metal-rich objects located in Figure 7 (toward higher  $[N II]\lambda 6583/H\alpha$  ratios); as we discuss below, this is not unexpected. The majority of the star-forming galaxies exhibit lower values of  $[N II]\lambda 6583/H\alpha$ , which is indicative of metal-poor systems.

It is important to stress that the inclusion of an emission-line object in the  $H\alpha$  Dots survey requires that the source be either extremely compact or unresolved at the resolution of our ground-based images (typical image quality of  $1''$ – $2''$ ). This dramatically impacts the make-up of our low-redshift  $H\alpha$ -detected sources. The  $H\alpha$  Dot survey does not catalog extended objects with large angular extents. Hence, luminous spiral disks with multiple H II regions are excluded from our lists, as are extended galaxies with strong nuclear starbursts. The natural outcome of this aspect of our selection function is that the  $H\alpha$ -detected components of the survey are typically low-luminosity star-forming dwarfs. This in turn explains the tendency for the  $H\alpha$ -detected objects to be located in the upper left-hand portion of the star-forming sequence in the BPT diagram.

The  $[O III]\lambda 5007$ -detected  $H\alpha$  Dots are separated into star-forming (solid green dots) and AGN (green triangles) components. The two classes of objects are cleanly separated in Figure 7. In all of the cases included in the plot, we made use of the G3 spectra that provide measurements of the  $[N II]\lambda 6583/H\alpha$  ratio. The AGN are all classified as Seyfert 2 galaxies, and all show largish  $[O III]\lambda 5007/H\beta$  ratios ( $\geq 6.0$ ). Due to the selection effects associated with our survey, we would not expect to detect systems with lower equivalent-width emission lines, such as LINERs (Heckman 1980). The  $[O III]\lambda 5007$ -detected star-forming galaxies all possess high-excitation spectra (with one exception). As mentioned earlier, their spectra are similar to the GP galaxies (e.g., Cardamone et al. 2009; Brunker et al. 2020) that were originally recognized by their green colors and compact morphologies during visual inspection of the SDSS survey images (Lintott et al. 2008). Their locations in the BPT diagram imply that many of them possess low metal abundances, which is typical of the GP galaxies.

One aspect of the distribution of objects in Figure 7 that is worth pointing out is the large spread in the “excitation” values ( $[O III]\lambda 5007/H\beta$  ratio) of the star-forming objects; that is, for a given value of the  $[N II]\lambda 6583/H\alpha$  ratio, the spread in  $[O III]\lambda 5007/H\beta$  is larger than is typically seen in samples of ELGs. For example, a comparison with Figure 1 in either Hirschauer et al. (2018) or Wegner et al. (2019), based on ELGs from the KISS objective-prism survey (Salzer et al. 2000, 2001; Gronwall et al. 2004), shows that many of the  $H\alpha$  Dots extend to much lower values of  $[O III]\lambda 5007/H\beta$ . This is typically interpreted as an age effect: lower excitation values indicate ionization from older stellar populations where the most massive O stars have already ended their lives. Apparently



the narrow-band survey method is more sensitive than the objective-prism search method, which allows for the detection of star-forming regions with a wider range of ages and properties.

### 5.3. Classification of Object Types

Based on the combination of spectroscopic and morphological information, we classify each of the H $\alpha$  Dots into one of the following classes of objects. Our classification scheme closely follows that used in Kellar et al. (2012). Here, we better define what we mean by each ELG class. The adopted classifications for each H $\alpha$  Dot are given in the second column of Table 2.

**Dwarf Star-forming Galaxies:** The majority of the H $\alpha$ -detected sources fall into the broad category of star-forming dwarf galaxies. As mentioned earlier, our selection criteria tend to restrict the choice of candidate H $\alpha$  emitting objects to be low-luminosity systems. The compactness criterion further tends to select low redshift H $\alpha$  Dots that could be classified as BCDs.

Visual inspection of the sample reveals that most, but not all, of the H $\alpha$ -detected Dots have properties that are consistent with the BCDs. There are a few notable exceptions. In a handful of cases (e.g., H $\alpha$  Dots 60, 127, 147) our narrow-band survey detected an H II region in a low surface brightness dwarf galaxy that was too faint to be visible in our short exposure *R*-band continuum images. While these are *bona fide* star-forming dwarf galaxies, they are not compact. Two other outliers in our sample are H $\alpha$  Dots 41 and 67. While these two galaxies exhibit very compact morphologies with extremely strong central emission, deeper broad-band imaging (e.g., SDSS) reveals that they have a more substantial underlying host galaxy than do most of the other H $\alpha$  Dots. Both have  $M_R \sim -18.5$ , making them by far the most luminous of the H $\alpha$ -detected Dots. For comparison, these absolute magnitudes lie approximately midway between the *R*-band luminosities of the Large and Small Magellanic Clouds.

With these exceptions aside, the vast majority of the H $\alpha$ -detected sources are BCD-like in nature, and may well constitute one of the best samples of such objects with distances out to  $\sim 100$  Mpc currently available. The locations of many of these galaxies in the BPT diagram (Figure 7) suggests that at least some of these BCDs are well past the peak in their star-forming episode.

**Outlying/Isolated H II Regions:** The H $\alpha$ -detected objects that do not fall into the star-forming dwarf galaxies category are all classified as outlying or isolated H II regions (e.g., Ryan-Weber et al. 2004; Werk et al. 2010). These are star-forming regions located beyond what appears to be the outer edge of their host galaxy.

We classify objects as outlying H II regions when they appear to be located close to a large galaxy and have brightnesses comparable to the brightest H II regions visible in that galaxy. They typically are very compact emission regions. While we will preliminarily assign an object to this category based on the survey imaging data, spectroscopic confirmation that the H II regions have velocities similar to their hosts is required before the classification can be formally adopted. These objects usually distinguish themselves as having much higher metal abundances than are typically seen in dwarf galaxies with comparable luminosities (see Section 5.4).

In a few cases, multiple outlying H II regions have been detected in the same galaxy. H $\alpha$  Dots 130 and 132–134 are all associated with the face-on barred spiral NGC 765, and are located well outside the main disk of the galaxy. H $\alpha$  Dots 103–106 are located in the faint outer ring of UGC 4599, which is the nearest Hoag-type ring galaxy known (Finkelman & Brosch 2011).

**GP-like Galaxies:** As mentioned earlier, the H $\alpha$  Dots survey is quite sensitive to galaxies with strong [O III] $\lambda$ 5007 emission in the redshift range 0.31–0.35. The [O III]-detected galaxies are typically Seyfert 2 galaxies ( $N = 16$ ) or star-forming galaxies with spectra similar to the so-called GP galaxies ( $N = 40$ ), such as those in Cardamone et al. (2009).

To distinguish between these two classes, we typically require the G3 spectra that provide access to the redshifted H $\alpha$  and [N II] lines. G3 spectra exist for all but one of the [O III]-detected galaxies discussed in the current study (the one exception is H $\alpha$  Dot 72), so that our current classifications are largely unambiguous. We note that none of the [O III]-detected SFGs shown in Figure 7 have  $\log([O III]/H\beta)$  values above 0.9, while none of the Seyfert 2 galaxies have  $\log([O III]/H\beta)$  less than 0.75. Hence, one can typically get a good inkling of the correct class of each [O III]-detected H $\alpha$  Dot without access to the [N II] $\lambda$ 6583/H $\alpha$  ratio, but the latter line ratio is essential for definitive classifications.

Many of the [O III]-detected SFGs have properties that are consistent with current samples of GP galaxies (e.g., Cardamone et al. 2009; Brunker et al. 2020) and are *bona fide* GPs. Others are less extreme in terms of their properties (e.g., lower SFRs, weaker spectra) and may simply be strongly star-forming galaxies at these intermediate redshifts. This will become more evident in Section 5.4. Hence, we will refer to these [O III]-detected SFGs as GP-like galaxies. Additional analysis of these objects is currently underway and will be reported in a separate study.

**Seyfert 2 Galaxies:** Due to the selection technique employed by this survey, all of the Seyfert 2 galaxies are [O III]-detected sources at intermediate redshifts (plus one [O II]-detected galaxy at  $z = 0.792$ ). Due to the compactness criterion mentioned earlier, no lower-redshift H $\alpha$ -detected sources could fall within this classification—nearby Seyfert galaxies are all large, extended systems.

The Seyfert classification method is primarily a spectroscopic method that is based on emission-line ratios that indicate photoionization from a nonstellar source of UV photons (e.g., Baldwin et al. 1981; Veilleux & Osterbrock 1987, see Figure 7). As with the GP-like galaxies, the existence of the G3 spectra is vital for unambiguous classification. While we possess G3 spectra for all of the Seyfert 2 galaxies, we note that the single [O II]-detected Seyfert 2, H $\alpha$  Dot 161, has its H $\alpha$  and [N II] lines redshifted beyond the range of the G3 spectral coverage. In this case, its classification rests primarily on the observed [O III]/H $\beta$  ratio. The  $\log([O III]/H\beta)$  value for this source is 0.82, which places it in the ambiguous region where the Seyfert 2 and high-excitation GP-like galaxies overlap. Given that the GP-like galaxies with such high [O III]/H $\beta$  ratios tend to have weak [O II] lines, we have tentatively classified this particular galaxy as a Seyfert 2 given that its [O II] lines were strong enough to allow detection.

**Seyfert 1 Galaxies and QSOs:** A primary classification criterion of Seyfert 1 galaxies and QSOs is the existence of broad emission lines of permitted transitions, such as the

**Table 3**  
H $\alpha$  Dots: Average Properties within ELG Classes

ELG Class (1)	Number (2)	$\langle z \rangle$ (3)	$\langle m_R \rangle$ (4)	$\langle M_R \rangle$ (5)	$\langle \text{SFR} \rangle$ (6)	$\langle \log(\text{O}/\text{H}) + 12 \rangle$ (7)
Dwarf SFGs	73	0.0154	18.73	−15.46	0.073	8.07
Outlying H II Regions	12	0.0128	21.00	−12.64	0.029	8.50
GP-like Galaxies	40	0.3416	20.68	−20.73	19.19	8.09
Seyfert 2 s	17	0.3625	19.76	−21.79	...	...
Seyfert 1 s	3	0.4987	19.35	−22.97	...	...
QSOs	9	3.1678	19.78	−27.42	...	...

Balmer series lines and Helium lines. In addition, QSOs are usually distinguished by their high optical luminosities. Because the forbidden metal lines and permitted lines emanate from different regions of the AGN, they are typically not plotted in BPT-like diagrams (hence their absence from Figure 7).

Once again, the compactness criterion used in selecting H $\alpha$  Dots eliminates the possibility of detecting any Seyfert 1 galaxies in the H $\alpha$ -detected subsample. Only three Seyfert 1 s have been identified by the survey to date: one is [O III]-detected ( $z = 0.3234$ ), the second is [O II]-detected ( $z = 0.7941$ ), and the third is H $\beta$ -detected ( $z = 0.3785$ ). The latter source is the only H $\alpha$  Dot found to date that is detected via the H $\beta$  line, and is included in the [O III]-detected group in the redshift histogram shown in Figure 6. Naturally, all of the Seyfert 1 galaxies exhibit broad permitted lines. Measured velocity widths (FWHM) for the three H $\alpha$  Dot Seyfert 1 s range between 2300 and 5000 km s<sup>−1</sup>.

The nine QSOs detected so far in the survey have all been detected via broad UV emission lines as detailed in Section 5.1. Their redshifts range from  $z = 1.35$  (Mg II detection) to  $z = 4.49$  (Ly $\alpha$  detection). Example spectra are displayed in Figure 5.

We summarize the object classifications of the complete set of H $\alpha$  Dots in Table 3. The table includes the number of objects discovered within each grouping (column 2) plus average values within each group for various observed and derived quantities: redshift (column 3), apparent R magnitude (column 4), absolute R magnitude (column 5), SFR (column 6) and metal abundance (column 7). The latter two quantities are naturally only presented for star-forming systems. We refer to the contents of this table in the following subsection.

#### 5.4. Properties of the H $\alpha$ Dots

In this subsection we illustrate the distribution of derived properties for the H $\alpha$  Dots and relate these results with the previous discussions of spectral properties and ELG classifications.

Figure 8 presents the distribution of *R*-band absolute magnitudes for the full sample of 154 unique H $\alpha$  Dots (i.e., duplicates and false detections excluded). The histograms are broken into three groups: H $\alpha$ -detected in red, which includes the dwarf star-forming galaxies and outlying H II regions; all intermediate-redshift objects detected via [O III] or [O II] lines (plus the single H $\beta$  detection) shown in green, which includes all of the Seyfert galaxies as well as the GP-like objects; high-redshift objects detected by one of the strong UV emission lines in blue, which encompasses the QSOs found in the survey.

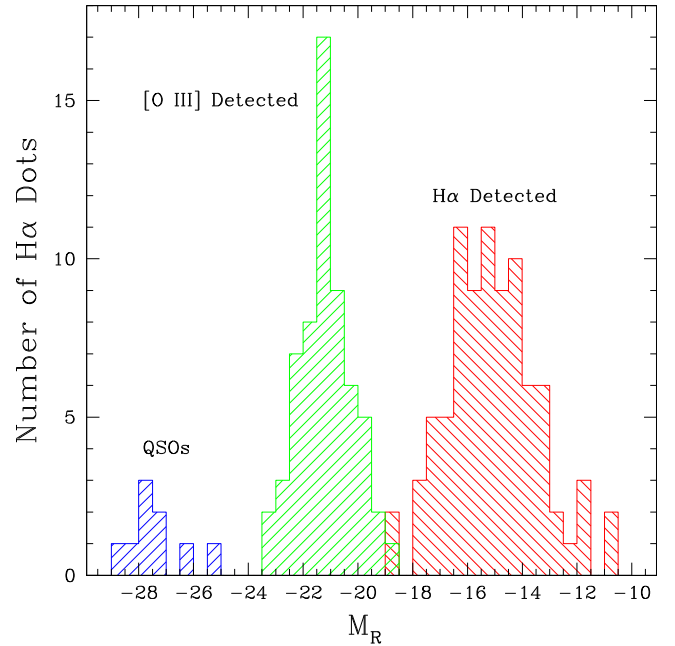


**Figure 8.** Distribution of *R*-band absolute magnitudes for the first two lists of H $\alpha$  Dots ( $N = 154$ ). Separate histograms are presented to the H $\alpha$ -detected Dots (red,  $N = 85$ ), which are a mix of dwarf compact star-forming galaxies and outlying H II regions, the [O III]- and [O II]-detected objects (green,  $N = 60$ ), which include both Seyfert and GP-like galaxies, and UV-line-detected QSOs (blue,  $N = 9$ ). The latter group all have absolute magnitudes more luminous than  $-25$ .

Even a cursory glance at Figure 8 reveals that the selection method used for the H $\alpha$  Dots survey leads to the creation of well-defined, essentially non-overlapping subsamples of the strong-lined galaxy population. The H $\alpha$ -detected objects are all lower luminosity systems, which is dictated by the low redshifts covered by the survey filters for the H $\alpha$  line combined with the compactness requirement. As seen in Table 3, the luminosities of the outlying H II regions trend toward the lowest luminosities in the sample, while the star-forming dwarf galaxies, which make up the largest subset of the H $\alpha$  Dots, exhibit a mean absolute magnitude nearly 3 magnitudes more luminous.

The intermediate-redshift galaxies (green histogram) is almost completely separate from the H $\alpha$ -detected systems in Figure 8, reflecting the high redshifts of the objects detected. The Seyfert galaxies dominate the more luminous end of the distribution here, with mean  $M_R$  of  $-22.97$  for the three Seyfert 1 s and  $-21.79$  for the 17 Seyfert 2 s. The GP-like galaxies cover a broad luminosity range, but dominate the numbers in the green histogram at values below  $-21$ . The simple fact that such a large fraction of the H $\alpha$  Dots are [O III]-detected at these

intermediate redshifts speaks both to the sensitivity of the survey method (the average  $m_R$  for the GP-like galaxies is 20.7) and to the importance of this class of galaxy at these redshifts (see also Brunker et al. 2020).

As one would expect, the QSOs stand apart from the other objects in the catalog in terms of their luminosities. Since our sample of QSOs is a small one, it is not possible to draw strong conclusions regarding it. Our sense is that, while the derived absolute magnitudes for the QSOs are consistent with other such objects, the QSOs found among the H $\alpha$  Dots tend to be among the more luminous. This would presumably be a result of the fact that, at a given redshift, only the more luminous examples would be detectable with our survey method given the small size of our telescope.

Next we consider the H $\alpha$  line luminosities and SFRs for the H $\alpha$  Dots. In all cases, the line luminosities are derived from the calibrated narrow-band imaging fluxes rather than from spectroscopic fluxes. This should result in more accurate SFR estimates, since no corrections for aperture effects are required. For the [O III]-detected sources, the total H $\alpha$  flux is derived using the observed narrow-band emission-line flux combined with the spectroscopic H $\alpha$ /[O III] ratio. The line fluxes for the H $\alpha$ -detected galaxies are corrected for the presence of [N II] emission within the filter bandpass, using the observed spectroscopic [N II]/H $\alpha$  ratio; in most cases this correction is small due to the weakness of the Nitrogen lines in the low-metallicity dwarfs. No similar correction is required for the [O III]-detected objects. The H $\alpha$  line fluxes are also corrected for absorption using the Balmer reddening coefficients ( $c_{H\beta}$ ) listed in Table 2. SFRs are computed from the derived H $\alpha$  luminosities using the standard Kennicutt (1998) relationship:

$$SFR [M_{\odot} \text{ yr}^{-1}] = 7.9 \times 10^{-42} L_{H\alpha}. \quad (3)$$

The values for  $L_{H\alpha}$  and SFR for the star-forming H $\alpha$  Dots are listed in the last two columns of Table 1.

The H $\alpha$ -based SFRs for all of the star-forming galaxies are shown in Figure 9. Once again, the lower-redshift H $\alpha$ -detected galaxies are shown as the red histogram, while the intermediate-redshift [O III]-detected Dots are shown in green. For this figure, we do not include the SFRs of the outlying H II regions, but rather focus on the *bona fide* galaxies. As was seen in the histogram of the absolute magnitudes, the SFR distributions of the H $\alpha$ - and [O III]-detected galaxies segregate completely in Figure 9.

The median SFR of the dwarf star-forming galaxies is  $0.024 M_{\odot} \text{ yr}^{-1}$ , substantially less the average value of  $0.073 M_{\odot} \text{ yr}^{-1}$  reported in Table 3. Whichever number is chosen to parameterize the characteristic SFR of the dwarf star-forming galaxies, it is clear that the typical values are on the high side for galaxies with these types of luminosities. This should be not surprise, given the way that the sample is selected. Comparison with the volume-limited 11HUGS survey (Lee et al. 2009, see their Figure 6) shows that a large majority of the latter sample of galaxies with  $M_B > -16$  (which corresponds roughly to  $M_R > -17$ ) have SFRs less than  $0.01 M_{\odot} \text{ yr}^{-1}$ . Fully 19% of the H $\alpha$  Dots star-forming dwarfs in Figure 9 have SFRs above  $0.1 M_{\odot} \text{ yr}^{-1}$ , compared to 0% of the galaxies with  $M_B > -16$  from the 11HUGS sample. Hence, as we suggested earlier, the dwarf SFG population cataloged by our survey method is effective at discovering many strongly star-forming dwarfs located within the boundaries of the AHA survey fields, even

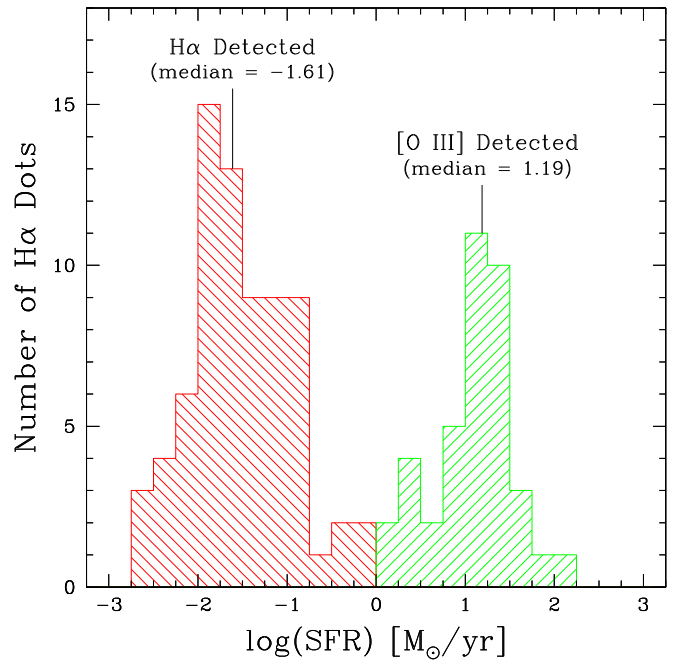


**Figure 9.** Distribution of SFRs for the star-forming component of the H $\alpha$  Dots. The red histogram shows the SFR distribution for the low-redshift H $\alpha$ -detected galaxies ( $N = 73$ ), which are predominantly dwarfs. The SFRs of the [O III]-detected Dots are shown in the green histogram ( $N = 39$ ), which includes systems with SFRs in excess of  $100 M_{\odot} \text{ yr}^{-1}$ . The median values of the two samples are indicated; they differ by a factor of 630. The [O III]-detected Dots include many GP galaxy candidates.

though these objects were not themselves AHA targets. Many of the dwarf SFGs could be classified as BCDs.

The [O III]-detected SFGs exhibit substantially higher SFRs compared with the dwarfs. The SFRs range from  $1\text{--}100+ M_{\odot} \text{ yr}^{-1}$ , with a median value of  $15.5 M_{\odot} \text{ yr}^{-1}$ . The median SFR for the GP-like galaxies is a factor of 630 times higher than the median for the dwarf SFGs! The range of SFR values found for previously published samples of GP galaxies falls between log (SFR) of 0.5 and 1.8 (Cardamone et al. 2009; Brunker et al. 2020). Hence, the majority of the [O III]-detected H $\alpha$  Dots that are SFGs are likely to be *bona fide* GPs.

The abundances for the H $\alpha$  Dots are derived utilizing the so-called O3N2 strong-lined abundance method (e.g., Alloin et al. 1979; Pettini & Pagel 2004; Pérez-Montero & Contini 2009; Marino et al. 2013). Here we adopt the O3N2 calibration derived by Hirschauer et al. (2018) for the KISS ELGs. Since the latter sample consists almost exclusively of high-excitation SFGs, the Hirschauer et al. (2018) calibration is only valid for galaxies close to the locus of high-excitation points that lie on the star-forming sequence in the BPT diagram (see Figure 1 of Hirschauer et al. 2018). This locus of points is well approximated by the theoretical curve from Dopita & Evans (1986) included in Figure 7. This curve in fact represents the highest excitation models computed by these authors.

Following the prescription presented in Hirschauer et al. (2018), we identify the H $\alpha$  Dots that are located sufficiently far from the high-excitation locus that their metallicity estimates would be questionable. These are the low-excitation objects that are located below the blue-dashed line in Figure 7. Most of the star-forming objects that exhibit low-excitation spectra are dwarf star-forming galaxies, although one [O III]-detected source and a few outlying H II region are also in this category. We do not report a metallicity estimate in Table 2 for these



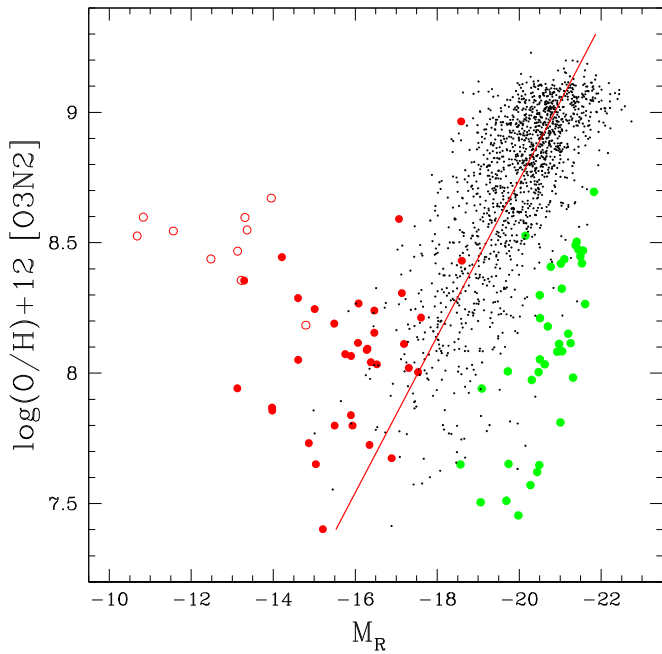


**Figure 10.** Luminosity-Metallicity (L-Z) plot for the  $H\alpha$  Dots. The colored symbols have the same meaning as those used in Figure 7. The small black dots are star-forming galaxies from KISS ( $N = 1450$ ), while the solid red line is a linear fit to the KISS L-Z relation. Both the  $H\alpha$  Dots designated as outlying H II regions and the [O III]-detected Dots are substantially offset from the KISS L-Z relation, as discussed in the text.

objects. In the end we derived reliable metallicity estimates for 35 dwarf SFGs, 10 outlying H II region, and 36 GP-like galaxies.

A luminosity-metallicity (LZ) relation plot for the star-forming  $H\alpha$  Dots is shown in Figure 10. The symbols have the same meaning as in Figure 7: filled red circles are  $H\alpha$ -detected dwarf SFGs, open red circles are outlying H II regions, and filled green circles are [O III]-detected GP-like galaxies. In addition, we plot star-forming galaxies with measured abundances from KISS (Hirschauer et al. 2018), shown as small dots. The latter sample is utilized to represent a typical L-Z relation for actively SFGs.

Examination of Figure 10 reveals that none of the  $H\alpha$  Dots galaxy subsamples closely follows the LZ relation defined by the KISS ELGs. For at least two of the subsamples, this was entirely expected. We consider each of the subsamples in turn.

The expectation is that the measured metal abundances for the outlying H II regions should reflect the metallicity level in the outer parts of their host galaxies (see Section 5.3). Since these H II regions are all associated with galaxies that are hundreds of times more luminous than the H II regions themselves, their metal abundances should be quite high. Hence, their locations in the LZ diagram should be substantially above the nominal relationship for real galaxies of similar luminosity. This is exactly what we observe in Figure 10. Most of the outlying H II regions shown in the LZ plot have O3N2 abundances of  $8.5 \pm 0.2$ , which place them between 1.5 and 2.0 dex above the extrapolation of the linear LZ relation fit to the KISS ELGs.

Typical GP and GP-like galaxies have metal abundances that are well below the LZ relation defined by normal galaxies (Cardamone et al. 2009; Izotov et al. 2011; Brunker et al. 2020). This is seen in Figure 10, where the [O III]-detected star-forming  $H\alpha$  Dots all fall below the linear LZ fit to the KISS

ELGs. In many cases the offset to lower abundances is modest; there is plenty of overlap between the parameter space occupied by the star-forming KISS galaxies and the GP-like  $H\alpha$  Dots. However, there are also a number of [O III]-detected systems that exhibit extreme offsets in Figure 10. These are likely genuine GPs.

While we expected the outlying H II regions and GP-like galaxies to not follow the LZ relation for the KISS ELGs, we had no reason to expect that the dwarf SFGs detected as  $H\alpha$  Dots would also show an offset from the relation. However, it is clear from Figure 10 that the dwarf SFGs are offset to higher abundances, on average, relative to the KISS LZ relation. Since the same method is used to derive the metal abundance for all galaxies shown in Figure 10, the offset cannot be attributed to differences in the abundance scales. Furthermore, the median redshift of the 34 dwarf SFGs in Figure 10 is  $4700 \text{ km s}^{-1}$ . Even with a large peculiar velocity of  $300 \text{ km s}^{-1}$ , a galaxy at the median redshift would only have its distance affected at the 6% level, not enough to account for the significant offsets observed. There are 27  $H\alpha$  Dots in the plot with  $M_R > -17$ , and all but one is above the linear fit line. The slope of the LZ fit to the KISS ELGs is dominated by the more numerous intermediate and high luminosity galaxies. Hence, the dwarf SFGs in the  $H\alpha$  Dot samples may be indicating that the slope of the LZ relation becomes shallower at lower luminosities. This possibility was previously suggested by Kellar et al. (2012) and Hirschauer et al. (2018), among others. We return to this issue in the next section.

### 5.5. Example Applications for the $H\alpha$ Dots

An extensive list of potentially interesting applications and follow-up projects for the  $H\alpha$  Dots was given in Kellar et al. (2012). Here we summarize three specific projects that utilize three different subsamples of the  $H\alpha$  Dots, in the hopes of illustrating the utility and versatility of the objects found in our survey.

**Direct Abundances of Dwarf SFGs:** As we have highlighted throughout this document, the  $H\alpha$  Dot selection method results in the detection of many low-luminosity star-forming galaxies in the volume of space covered by our narrow-band filters. Our survey preferentially detects strong-lined galaxies, which makes them excellent candidates for detailed abundance work. Our “quick-look” spectra have neither the spectral coverage nor the depth to allow us to derive accurate metallicities with these initial confirming spectra. However, we have been acquiring abundance-quality spectra for the most interesting targets as opportunity has allowed. To date, we have collected spectra for roughly two dozen dwarf SFGs from the  $H\alpha$  Dots lists that exhibit the temperature-sensitive [O III] $\lambda 4363$  line. Analysis of these spectra is well underway, and will result in the determination of “direct” abundances for a large sample of dwarf  $H\alpha$  Dots (A. Hirschauer et al. 2020, in preparation). Armed with these more accurate abundances, we plan to explore more vigorously the question of the possible slope change in the LZ relation referred to above.

**Properties of GP Galaxies:** It is abundantly clear that the  $H\alpha$  Dots survey is an excellent source of large numbers of previously unrecognized GP galaxies (Cardamone et al. 2009). As recent studies have shown, these objects are important for our understanding of extreme star-forming systems of the type that may be responsible for contributing to the re-ionization of the universe at  $z > 6$  (e.g., Henry et al. 2015; Izotov et al.

2016a, 2016b, 2017, 2018, 2020; Jaskot et al. 2017, 2019; Verhamme et al. 2017; Yang et al. 2017). In addition, the GPs appear to be among the most rapidly evolving galaxy population observed (Brunker et al. 2020). Hence, studying their properties at as many redshifts as possible is important.

The H $\alpha$  Dots survey detects GPs in the redshift range 0.31–0.35, which represents the outer limit of the Cardamone et al. (2009) sample. Members of the H $\alpha$  Dots survey team have begun detailed studies of these interesting and enigmatic objects. We are obtaining high quality spectra for direct abundances for many of the GP candidates. In addition, we are exploring the spatial distributions of galaxies in the vicinity of these GPs with the goal of understanding their environments (S. Brunker 2020, in preparation). We note that the H $\alpha$  Dots survey represents an emission-line flux-limited sample of galaxies with a quantifiable completeness limits. Hence, we will be able to derive reliable volume densities of the GP galaxies, which will allow us to better understand their evolution with lookback time as well as their contribution to the total SFR density at their observed redshifts.

**Volume Densities and Abundances of Intermediate Redshift Seyfert 2 Galaxies:** The [O III]-detected H $\alpha$  Dots also include a well-defined sample of Seyfert 2 galaxies that is located in the same redshift range as the GPs that we discussed earlier. Once again, the nature of the survey will allow us to measure accurate volume densities of strong-lined Seyfert 2s in the  $z = 0.31$ – $0.35$  range. This redshift range lies beyond the limits of current wide-field redshift surveys (e.g., none of the 17 H $\alpha$  Dot Seyfert 2s has been observed spectroscopically by SDSS), which allows us to push the census of strong-lined AGN to larger distances. In addition, preliminary evidence suggests that at least some of the [O III]-detected Seyfert 2 galaxies may have significantly lower metal abundances than their low redshift counterparts. This is seen in Figure 7, where a number of the H $\alpha$  Dot Seyfert 2s have lower values of [N II]/H $\alpha$  than are typically observed in local systems. For example, none of the large sample of nearby Seyfert 2s studied by Carvalho et al. (2020) have  $\log([N II]/H\alpha)$  below  $-0.4$ , while 6 of 16 of the H $\alpha$  Dot Seyfert 2s have values below this limit. We are currently exploring methods to derive reliable abundances for Seyfert 2 galaxies (D. Carr 2020, in preparation), with an eye toward evaluating any possible evolution with lookback time.

## 6. Summary and Conclusions

We present a second list of point-like emission-line objects known as H $\alpha$  Dots. These objects were discovered serendipitously by carrying out systematic searches of hundreds of narrow-band images obtained for the ALFALFA H $\alpha$  project (Van Sistine et al. 2016).

A total of 354 fields were searched, resulting in the discovery of 119 compact/unresolved emission-line candidates (112 unique objects after accounting for duplications due to field overlap). Our imaging data yield  $R$ -band magnitudes and calibrated emission-line fluxes for all ELG candidates. In addition, all of our candidates have been observed spectroscopically. We present redshifts and emission-line diagnostics for all of our newly detected objects. These spectra reveal the nature of the objects being cataloged. In particular, they show that our survey method is sensitive to the detection of objects via a variety of emission lines: H $\alpha$ , [O III] $\lambda$ 5007, H $\beta$ , [O II] $\lambda$ 3727, and several UV emission lines commonly observed in QSOs, including Ly $\alpha$ .

We combine and analyze all 180 H $\alpha$  Dots from the first two survey lists to develop a more comprehensive picture of the make-up of our ELG sample. We are able to categorize this apparently heterogeneous group of strong-lined sources into just five classes of galaxies with activity: dwarf star-forming galaxies (including many BCDs), outlying/isolated H II regions, GP-like galaxies, Seyfert 2 galaxies, and broad-line AGN (mostly QSOs). Our narrow-band selection method concentrates these classes into specific redshift windows, depending on the emission line that is used in their selection. This means that the individual H $\alpha$  Dot categories represent samples of both line-flux-limited and redshift-limited galaxies. We utilize the available observational data to explore the properties of the galaxies in each of these groups






The H $\alpha$  Dots survey project is ongoing and continues to be carried out primarily by undergraduate research students. Additional lists of H $\alpha$  Dots are being prepared for publication (e.g., D. Watkins 2020, in preparation), and our program of follow-up spectroscopy is continuing. We are also pursuing detailed studies of specific subsamples of the H $\alpha$  Dots, as highlighted in Section 5.5. In addition to generating more survey lists of new ELG candidates, future papers in this series will derive detailed metallicities of the dwarf star-forming H $\alpha$  Dots, explore the properties of the GP galaxies found in the survey, and analyze the population of intermediate-redshift Seyfert 2 galaxies uncovered by this work.

We thank the anonymous referee for making numerous suggestions that greatly improved the presentation of this paper. We gratefully acknowledge the financial support of the College of Arts and Sciences and the Department of Astronomy at Indiana University, which made our access to the WIYN 0.9 m telescope possible. The H $\alpha$  Dots survey project is based on data obtained for the ALFALFA H $\alpha$  project, which was carried out with the support of the National Science Foundation (NSF-AST-0823801).

This project made use of Sloan Digital Sky Survey data. Funding for the SDSS and SDSS-II has been provided by the Alfred P. Sloan Foundation, the Participating Institutions, the National Science Foundation, the U.S. Department of Energy, the National Aeronautics and Space Administration, the Japanese Monbukagakusho, the Max Planck Society, and the Higher Education Funding Council for England. The SDSS Web Site is <http://www.sdss.org/>. The SDSS is managed by the Astrophysical Research Consortium for the Participating Institutions. The participating institutions are the American Museum of Natural History, Astrophysical Institute Potsdam, University of Basel, University of Cambridge, Case Western Reserve University, University of Chicago, Drexel University, Fermilab, the Institute for Advanced Study, the Japan Participation Group, Johns Hopkins University, the Joint Institute for Nuclear Astrophysics, the Kavli Institute for Particle Astrophysics and Cosmology, the Korean Scientist Group, the Chinese Academy of Sciences (LAMOST), Los Alamos National Laboratory, the Max-Planck-Institute for Astronomy (MPIA), the Max-Planck-Institute for Astrophysics (MPA), New Mexico State University, Ohio State University, University of Pittsburgh, University of Portsmouth, Princeton University, the United States Naval Observatory, and the University of Washington.

*Facilities:* WIYN:0.9 m, HET(LRS).

## ORCID iDs

John J. Salzer  <https://orcid.org/0000-0001-8483-603X>  
 Jesse R. Feddersen  <https://orcid.org/0000-0003-3810-3323>  
 Caryl Gronwall  <https://orcid.org/0000-0001-6842-2371>  
 Steven Janowiecki  <https://orcid.org/0000-0001-9165-8905>  
 Alec S. Hirschauer  <https://orcid.org/0000-0002-2954-8622>

## References

- Abolfathi, B., Aguado, D. S., Aguilar, G., et al. 2018, *ApJS*, **235**, 42  
 Alloin, D., Collin-Souffrin, S., Joly, M., et al. 1979, *A&A*, **78**, 200  
 Baldwin, J. A., Phillips, M. M., & Terlevich, R. 1981, *PASP*, **93**, 5  
 Bennett, A. S. 1962, *MmRAS*, **68**, 163  
 Boroson, T. A., Salzer, J. J., & Trotter, A. 1983, *ApJ*, **412**, 524  
 Brunker, S. W., Salzer, J. J., Janowiecki, S., et al. 2020, *ApJ*, **898**, 68  
 Cardamone, C., Schawinski, K., Sarzi, M., et al. 2009, *MNRAS*, **399**, 1191  
 Carvalho, S. P., Dors, O. L., Cardaci, M. V., et al. 2020, *MNRAS*, **492**, 5675  
 Cook, D. O., Kasliwal, M. M., Van Sistine, A., et al. 2019, *ApJ*, **880**, 7  
 Dopita, M. A., & Evans, I. N. 1986, *ApJ*, **307**, 431  
 Edge, D. O., Shakeshaft, J., McAdam, W., et al. 1959, *MmRAS*, **68**, 37  
 Finkelman, I., & Brosch, N. 2011, *MNRAS*, **413**, 2621  
 Giovanelli, R., Haynes, M. P., Kent, B. R., et al. 2005, *AJ*, **130**, 2598  
 Gronwall, C., Salzer, J. J., Sarajedini, V. L., et al. 2004, *AJ*, **127**, 1943  
 Haynes, M. P., Giovanelli, R., Kent, B. R., et al. 2018, *ApJ*, **861**, 49  
 Haynes, M. P., Giovanelli, R., Martin, A. M., et al. 2011, *AJ*, **142**, 170  
 Heckman, T. M. 1980, *A&A*, **87**, 152  
 Henry, A., Scarlata, C., Martin, C. L., et al. 2015, *ApJ*, **809**, 19  
 Hill, G. J., Nicklas, H. E., MacQueen, P. J., et al. 1998, *Proc. SPIE*, **3355**, 375  
 Hirschauer, A. S., Salzer, J. J., Janowiecki, S., et al. 2018, *AJ*, **155**, 82  
 Hopp, U., Engels, D., Green, R. F., et al. 2000, *A&AS*, **142**, 417  
 Izotov, Y. I., Guseva, N. G., & Thuan, T. X. 2011, *ApJ*, **728**, 161  
 Izotov, Y. I., Orlitová, I., Schaerer, D., et al. 2016a, *Natur*, **529**, 178  
 Izotov, Y. I., Schaerer, D., Thuan, T. X., et al. 2016b, *MNRAS*, **461**, 3683  
 Izotov, Y. I., Schaerer, D., Worseck, G., et al. 2018, *MNRAS*, **474**, 4514  
 Izotov, Y. I., Schaerer, D., Worseck, G., et al. 2020, *MNRAS*, **491**, 468  
 Izotov, Y. I., Thuan, T. X., & Guseva, N. G. 2017, *MNRAS*, **471**, 548  
 Jaskot, A. E., Dowd, T., Oey, M. S., et al. 2019, *ApJ*, **885**, 96  
 Jaskot, A. E., Oey, M. S., Scarlata, C., et al. 2017, *ApJL*, **851**, L9  
 Kakazu, Y., Cowie, L. L., & Hu, E. M. 2007, *ApJ*, **668**, 853  
 Kauffmann, G., Heckman, T. M., Tremonti, C., et al. 2003, *MNRAS*, **346**, 1055  
 Kellar, J. A., Salzer, J. J., Wegner, G., et al. 2012, *AJ*, **143**, 145  
 Kennicutt, R. C., Jr. 1998, *ARA&A*, **36**, 189  
 Laing, R. A., Riley, J. M., & Longair, M. S. 1983, *MNRAS*, **204**, 151  
 Lee, J. C., Kennicutt, R. C., Jr., Funes, J. G., et al. 2009, *ApJ*, **692**, 1305  
 Lintott, C. J., Schawinski, K., Slosar, A., et al. 2008, *MNRAS*, **389**, 1179  
 MacAlpine, G. M., Smith, S. B., & Lewis, D. W. 1977, *ApJS*, **34**, 95  
 MacAlpine, G. M., & Williams, G. A. 1981, *ApJS*, **45**, 113  
 Marino, R. A., Rosales-Ortega, F. F., Sánchez, S. F., et al. 2013, *A&A*, **559**, A114  
 Markarian, B. E. 1967, *Afz*, **3**, 55  
 Markarian, B. E., Lipovetskii, V. A., & Stepanian, D. A. 1981, *Afz*, **17**, 619  
 Markarian, B. E., Lipovetskii, V. A., & Stepanian, D. A. 1983, *Afz*, **19**, 29  
 Pérez-Montero, E., & Contini, T. 2009, *MNRAS*, **398**, 949  
 Pesch, P., & Sanduleak, N. 1983, *ApJS*, **51**, 171  
 Pettini, M., & Pagel, B. E. J. 2004, *MNRAS*, **348**, L59  
 Ryan-Weber, E. V., Meurer, G. R., Freeman, K. C., et al. 2004, *AJ*, **127**, 1431  
 Salzer, J. J., Gronwall, C., Lipovetsky, V. A., et al. 2000, *AJ*, **120**, 80  
 Salzer, J. J., Gronwall, C., Lipovetsky, V. A., et al. 2001, *AJ*, **121**, 66  
 Salzer, J. J., Gronwall, C., Sarajedini, V. L., et al. 2002, *AJ*, **123**, 1292  
 Sanduleak, N., & Pesch, P. 1982, *ApJL*, **258**, 11  
 Ugryumov, A. V., Engels, D., Lipovetsky, V. A., et al. 1999, *A&AS*, **135**, 511  
 van Dokkum, P. 2001, *PASP*, **113**, 1420  
 van Sistine, A., Salzer, J. J., Sugden, A., et al. 2016, *ApJ*, **824**, 25  
 Veilleux, S., & Osterbrock, D. E. 1987, *ApJS*, **63**, 295  
 Verhamme, A., Orlitová, I., Schaerer, D., et al. 2017, *A&A*, **597**, A13  
 Wasilewski, A. J. 1983, *ApJ*, **272**, 68  
 Wegner, G. A., Salzer, J. J., Taylor, J. M., et al. 2019, *ApJ*, **883**, 29  
 Werk, J. K., Putman, M. E., Meurer, G. R., et al. 2010, *AJ*, **139**, 279  
 Yang, H., Malhotra, S., Gronke, M., et al. 2017, *ApJ*, **844**, 171  
 York, D. G., Adelman, J., Anderson, J. E., et al. 2000, *AJ*, **120**, 1579  
 Zamorano, J., Gallego, J., Rego, M., et al. 1996, *ApJS*, **105**, 343  
 Zamorano, J., Rego, M., Gallego, J., et al. 1994, *ApJS*, **95**, 387